INRIA

UNITE DE RECHERCHE
INRIA ROCQUENCOURT

Institut National
de Recherche
en Informatique
et en Automatique

Domaine de Voluceau
Rocquencourt
BP 105
78153 Le Chesnay Cedex
France
Tel (1) 39635511

Rapports de Recherche

N° 1403

Programme 4
Robotique, Image et Vision

INTRODUCING DEFORMABLE SURFACES TO SEGMENT 3D IMAGES AND INFER DIFFERENTIAL STRUCTURES

Isaac COHEN
Laurent D. COHEN
Nicholas AYACHE

Mars 1991

Introducing deformable surfaces to segment 3D images and infer differential structures[1]

Isaac COHEN[2]
INRIA, Domaine de Voluceau,Rocquencourt B.P. 105, 78153 Le Chesnay CEDEX, France.
Email: isaac@bora.inria.fr, Tel.1-39 63 53 66
Laurent D. COHEN
CEREMADE, U.R.A. CNRS 749, Université Paris IX - Dauphine
Place du Marechal de Lattre de Tassigny 75775 Paris CEDEX, France.
Email: cohen@bora.inria.fr
Nicholas AYACHE
INRIA, Domaine de Voluceau,Rocquencourt B.P. 105, 78153 Le Chesnay CEDEX, France.
Email na@bora.inria.fr, Tel.1-39 63 53 20

[1]This work was partially supported by Digital Equipement Corporation and by European Advanced Informatics in Medicine contract MURIM.

[2]Boursier MRT, Université Paris IX - Dauphine

Abstract

In this paper, we introduce a *really 3-D* deformable model, which evolves in *true 3-D* images, under the action of internal forces (describing some elasticity properties of the surface), and external forces attracting the surface toward some detected edgels. Our formalism leads to the minimization of an energy which is expressed as a functional. We use a variational approach and a finite element method to actually express the surface in a discrete basis of continuous functions. This leads to a reduced computational complexity and a better numerical stability.

The power of the approach to segment 3-D images is demonstrated by a set of experimental results on various complex medical 3-D images.

Another contribution of this approach is the possibility to infer easily the differential structure of the segmented surface. As we end-up with an analytical description of class C^∞ of the surface almost everywhere, this allows to compute for instance its first and second fundamental forms. From this, one can extract a curvature primal sketch of the surface, including some intrinsic features like parabolic lines, extrema of curvatures, umbilic points etc..., which can be used as landmarks for 3-D image interpretation.

Utilisation de surfaces déformables pour segmenter des images 3D et en déduire les caracteristiques differentielles

Résumé

Dans cet article nous définissons un modèle déformable 3D qui évolue dans des images tridimensionnelles sous l'action de forces internes (décrivant les propriétés élastiques de la surface) et de forces externes attirant la surface vers les contours. La modélisation de ces forces définie une fonctionnelle d'énergie à minimiser. Une approche variationnelle et des éléments finis conformes sont utilisés pour decomposer la surface dans une base de fonctions continues. Ceci permet une meilleure stabilité numérique et réduit la compléxité algorithmique.

La fiabilité de cette approche pour la segmentation 3-D est illustrée par plusieurs resultats experimentaux obtenus à partir d'images médicales tridimensionnelles.

Un autre avantage de cette méthode est la possibilité de déduire la structure differentielle de la surface segmentée grâce à la description analytique (C^∞ presque partout) de la surface. Cela nous permet de calculer la première et seconde forme fondamentale de la surface et ainsi extraire les caracteristiques intrinsèques de celle-ci, telles que les lignes paraboliques, extrema de courbures, points ombiliques etc..., qui seront utilisées comme point de repère à l'interpretation d'images 3-D.

1 Introduction

We propose a deformable 3-D shape model which can be used to extract reliable surfaces in 3-D images and infer a differential structure on them.

Usually, 3-D images are given as a set of intensity voxels (volume elements). A 3-D edge detector, after a *local* image analysis [13, 19], provides a set of 3-D edgels (edge elements). These edgels can be considered as the trace of a certain number of surfaces trace.

One is then confronted with a dual problem :

1. select edgels belonging to the same surface trace; this is the segmentation problem.
2. recover a continuous and differentiable description of each surface; this yields an interpolation between the original sparse discrete data and the possibility to compute a differential structure useful for interpretation [1].

Both questions were analyzed by [16] who proposed to solve (1) by a connectivity analysis and (2) by the fitting of a set of local quadratic models. But difficulties arise when the connectivity analysis fails because edges are too sparse, and also when the model is too local to reliably describe a complex shape.

Another approach to solve a similar problem in 2-D consists in introducing an active deformable model [12], which solves the segmentation problem (1) assuming an initial estimate is provided [1] and the interpolation problem (2) when the curve is expressed in a basis of continuous functions [8, 14]. Such models were generalized in $2\frac{1}{2}$-D and 3-D by [18, 17] where the deformable surface is constrained as a surface of revolution evolving under the forces computed on a 2-D image or a set of 2-D images.

In this paper, we introduce a *really 3-D* deformable model, which evolves in *true 3-D* images, under the action of internal forces (describing some elasticity properties of the surface), and external

[1] An initial solution might be provided by several means, including user-interactivity, which is usually encouraged in medical applications.

forces attracting the surface toward some detected edgels. Our formalism leads to the minimization of an energy which is expressed as a functional. We use a variational approach and a finite element method to actually express the surface in a discrete basis of continuous functions. This method allows us to do an "adaptative subdivision" of the parametrization domain without adding nodal points and consequently without increasing the size of the linear system we solve. This leads to a reduced computational complexity and a better numerical stability than the finite difference method.

The power of the approach to segment 3-D images is demonstrated by a set of experimental results on various complex medical 3-D images.

Another contribution of this approach is the possibility to infer easily the differential structure of the segmented surface. As we end-up with an analytical description of class $\mathcal{C}^\infty$ of the surface almost everywhere[2], this allows to compute for instance its first and second fundamental forms [10]. From this, one can extract a curvature primal sketch of the surface [15, 4], including some intrinsic features like parabolic lines, extrema of curvatures, umbilic points etc..., which can be used as landmarks for 3-D image interpretation [2].

Last but not least, a careful analysis of our external forces (those which attract the deformable surface toward the edges) shows some intriguing connections with the properties of minimal surfaces : under certain conditions, the deformable surface should behave like a minimal surface, i.e. a surface whose mean curvature is null everywhere. We should investigate this point further in the near future.

The paper is organized as follows: We first define the 3D deformable model and then give an appropriate external force and his relationship with 3D edge points. We show then, how to

[2]except between 2 finite element patches, where the representation is only of class $\mathcal{C}^1$, i.e. the tangent plane is continuous.

solve this minimization problem by a finite element method. Finally we indicate how to infer the differential structure of the 3D images from the obtained surface.

2 Energy Minimizing Surfaces

We need a surface model on which we can act and control its shape depending on the nature of the 3D image data we are trying to fit, while having an accurate localization of the surface boundaries.

A model which provides these two features is the deformable surface model [17, 18]. This model is defined by a space of admissible deformations Ad and a functional E to minimize. This functional E represents the energy of the model. A surface v is defined by a mapping:

$$\Omega = [0,1] \times [0,1] \rightarrow R^3$$

$$(s,r) \mapsto v(s,r) = (x(s,r), y(s,r), z(s,r))$$

and the associated energy E is given by:

$$E : Ad \rightarrow R$$

$$v \mapsto E(v) = \int_\Omega w_{1,0} \left|\frac{\partial v}{\partial s}\right|^2 + w_{0,1} \left|\frac{\partial v}{\partial r}\right|^2 + 2w_{1,1} \left|\frac{\partial^2 v}{\partial s \partial r}\right|^2 + w_{2,0} \left|\frac{\partial^2 v}{\partial s^2}\right|^2 + w_{0,2} \left|\frac{\partial^2 v}{\partial r^2}\right|^2 + P(v(s,r))ds\,dr$$

where P is the potential associated to the external forces. The external forces refer to the forces which will allow the surface to localize the image attributes. So, if we want the surface to be attracted by 3D edge points, the potential P has to depend on the 3D gradient image. While the internal forces represent the forces acting on the shape of the surface. They depend on the coefficients $w_{i,j}$ which determine the elasticity (w_{10},w_{01}), the rigidity (w_{20},w_{02}) and the twist ($w_{1,1}$), i.e. the mechanical properties of the surface. We can also constrain the surface structure (like the wrapping) by chosing different types of boundary conditions (for instance, to create a cylinder or a torus).

A local minimum v of E satisfies the associated Euler-Lagrange equation:

$$\begin{cases} -\frac{\partial}{\partial s}\left(w_{1,0}\frac{\partial v}{\partial s}\right) - \frac{\partial}{\partial r}\left(w_{0,1}\frac{\partial v}{\partial r}\right) + 2\frac{\partial^2}{\partial s \partial r}\left(w_{1,1}\frac{\partial^2 v}{\partial s \partial r}\right) + \frac{\partial^2}{\partial s^2}\left(w_{2,0}\frac{\partial^2 v}{\partial s^2}\right) + \frac{\partial^2}{\partial r^2}\left(w_{0,2}\frac{\partial^2 v}{\partial r^2}\right) = -\nabla P(v) \\ + \textit{Boundary Conditions} \end{cases} \tag{1}$$

which represents the necessary condition for the minimum ($E'(v) = 0$). A solution of equation (1) can be seen either as realizing the equilibrium between internal and external forces or reaching the minimum of the energy E.

Since the energy function is not convex, there may be many local minima of E. The Euler-Lagrange equation (1) may characterize any such local minimum. But as we are interested in finding a 3D contour in a given area, we assume in fact that we have a rough *prior* estimation of the surface. This estimation is used to solve the associated evolution equation in which we add a temporal parameter t:

$$\begin{cases} \frac{\partial v}{\partial t} - \frac{\partial}{\partial s}\left(w_{1,0}\frac{\partial v}{\partial s}\right) - \frac{\partial}{\partial r}\left(w_{0,1}\frac{\partial v}{\partial r}\right) + 2\frac{\partial^2}{\partial s \partial r}\left(w_{1,1}\frac{\partial^2 v}{\partial s \partial r}\right) + \frac{\partial^2}{\partial s^2}\left(w_{2,0}\frac{\partial^2 v}{\partial s^2}\right) + \frac{\partial^2}{\partial r^2}\left(w_{0,2}\frac{\partial^2 v}{\partial r^2}\right) = -\nabla P(v) \\ v(0,s,r) = v_0(s,r) \text{ initial estimation} \\ + \textit{Boundary Conditions} \end{cases} \tag{2}$$

A solution to the static problem is found when the previous solution $v(t)$ stabilizes. Then the term $\frac{\partial v}{\partial t}$ vanishes, thus providing a solution of the static problem.

3 Fixing up the potential P

The potential P is such that the force $F(v) = -\nabla P(v)$ has to attract the surface to the image attributes we are looking for. Our main goal is the extraction of "good" edge points (i.e. to be able to remove spurious edge points, while insuring connected contours). Thus the surface has to

be attracted by edge points and those points must minimize the energy:

$$E_{ext} = \int\int P(v(s,r))dsdr \tag{3}$$

For this purpose we set the potential $P = -|\nabla \mathcal{I}|^2$ so that edge points will minimize E_{ext}, where $\mathcal{I}$ is the 3D image convolved with a gaussian function. But for numerical stability (a complete discussion is given in [7, 8]) the force is normalized as:

$$F(v) = -k\frac{\nabla P}{\| \nabla P \|}.$$

where k is a parameter which allows to tune the attraction force. Now, all the edge points including spurious ones have the same ability to attract the surface. But spurious points generally form small connected components in 3D images; consequently, when the surface converges towards the real contours, all these points first attract the surface and then are ignored by the regularization effect of the algorithm.

Another way to make the edge points attract the surface is using a Chamfer distance defined in [3] or an Euclidean distance [9] image. This image is obtained by computing the distance from edge points to every image point. These distances allow to compute at each image point the attraction force to the nearest edgels and consequently produce a faster convergence. For instance

$$P(v(s,r)) = -e^{-d(v(s,r))^2}$$

produce a slow convergence whereas

$$P(v(s,r)) = \frac{-1}{d(v(s,r))} \quad \text{and} \quad P \equiv -1 \text{ if } d(v(s,r)) = 0$$

produce a faster convergence ($d(v(s,r))$ denotes the distance between $v(s,r)$ and the nearest edge whereas the smallest distance between two distinct points is one pixel).

4 Minimizing surfaces and 3D image edge points

In the previous section we showed how to choose correctly the potential P such that the surface will localize accurately the edge points. Here we comment on the relationship between the surface minimizing the energy of external forces E_{ext} and 3D edge points.

$$E_{ext} = \int\int P(x(s,r))dsdr = -\int\int |\nabla \mathcal{I}(x(s,r))|\, dsdr$$

First we recall the definition of the 3D edges [5].

Definition: A 3D edge is a surface $\mathcal{S}$ whose points have a maximal gradient magnitude in the direction normal to the surface. All points along the surface $\mathcal{S}$ (called Canny's edge points) satisfy:

$$\frac{d\,|\nabla \mathcal{I}(x(s,r))|}{dN(x(s,r))} = 0 \tag{4}$$

where $N(x(s,r))$ is the normal to the surface $\mathcal{S}$ parametrized by the application $x(s,r)$ and $\mathcal{I}$ is the image $I(x,y,z)$ convolved with a gaussian.

To establish the relation between the energy minimizing surfaces and this definition, we define the energy associated to the external forces as

$$E_P(\mathcal{S}) = -\frac{1}{|\mathcal{S}|}\int\int |\nabla \mathcal{I}(x(s,r))|\, dsdr \tag{5}$$

where $|\mathcal{S}| = \int\int dsdr$.

In the appendix we show that a surface $\mathcal{S}$ is a local minimum of E_P, with respect to infinitesimal deformation, if:

$$\frac{d\,|\nabla \mathcal{I}(x(s,r))|}{dN(x(s,r))} = \frac{eG+gE}{EG}\left(|\nabla \mathcal{I}(x(s,r))| - \frac{1}{|\mathcal{S}|}\int\int |\nabla \mathcal{I}(x(s,r))|\, dsdr\right) = 0, \tag{6}$$

where $E(s,r)$, $G(s,r)$, $e(s,r)$ and $g(s,r)$ are the coefficients of the first and second fundamental forms in the basis $\{x_s, x_r\}$ (we use the same notations as in [10]). A similar result for planar

curves was shown in [11]. A remarkable result is that the fraction $\frac{eG+gE}{EG}$ is nothing else than the mean curvature of the surface $\mathcal{S}$, if we use an orthogonal parametrization.

Equation (6) shows that there exists two very interesting specific situations:

1. minimal surfaces (i.e. surfaces with a mean-curvature which is null everywhere),
2. surfaces whose trace is made of edgels with constant gradient magnitude (in this case, the term within parentheses vanishes in equation (6)).

In effect, in both cases, the second member of equation (6) vanishes to zero, which means that Canny's edge points coincide with the minimal external energy of a deformable model (if the parametrization remains orthogonal).

In practice these are interesting but exceptional academic situations, and the deformable model simply converges toward a solution which is an equilibrium between the applied external forces (corresponding to the energy E_P) and the internal forces, parametrized by the elasticity coefficients $w_{i,j}$.

If the surface has cyclic conditions (as it is the case for cylinders or torus), we have two additional equations:

$$|\nabla \mathcal{I}(\boldsymbol{x}(L,r))| = |\nabla \mathcal{I}(\boldsymbol{x}(0,r))| = \frac{1}{|\mathcal{S}|}\int\int |\nabla \mathcal{I}(\boldsymbol{x}(s,r))|\, dsdr \quad \forall r \in [0,M] \tag{7}$$

$$|\nabla \mathcal{I}(\boldsymbol{x}(s,M))| = |\nabla \mathcal{I}(\boldsymbol{x}(s,0))| = \frac{1}{|\mathcal{S}|}\int\int |\nabla \mathcal{I}(\boldsymbol{x}(s,r))|\, dsdr \quad \forall s \in [0,L] \tag{8}$$

where $\Omega = [0,L] \times [0,M]$.

5 Numerical solution by finite elements

We consider the same evolution equation as in the previous section:

$$\begin{cases} \frac{\partial v}{\partial t} - \frac{\partial}{\partial s}\left(w_{1,0}\frac{\partial v}{\partial s}\right) - \frac{\partial}{\partial r}\left(w_{0,1}\frac{\partial v}{\partial r}\right) + 2\frac{\partial^2}{\partial s \partial r}\left(w_{1,1}\frac{\partial^2 v}{\partial s \partial r}\right) + \frac{\partial^2}{\partial s^2}\left(w_{2,0}\frac{\partial^2 v}{\partial s^2}\right) + \frac{\partial^2}{\partial r^2}\left(w_{0,2}\frac{\partial^2 v}{\partial r^2}\right) = -\nabla P(v) \\ v(0,s,r) = v_0(s,r) \text{ initial estimation} \\ + \textit{Boundary Conditions} \end{cases} \tag{9}$$

In the following, to simplify the notations, we consider the equation (9) with null boundary conditions (this is done by a simple change of variables).

We solve this last equation using a Finite Elements Method (FEM) [6]. The main idea of the FEM is to approximate over the Sobolev space $H_0^2(\Omega)$ the solution of the associated variational problem: find $v \in H_0^2(\Omega)$ such that

$$a(v,\varphi) = L(\varphi) \quad \forall \varphi \in H_0^2(\Omega) \tag{10}$$

where L is assumed to be independent of v (see appendix for details). There exists a unique solution to this equation, since the bilinear form $a(\varphi,\psi)$ is symmetric and positive definite as long as $w_{k,l}(s,r) > 0$.

A well-known approach for approximating such problems is Galerkin's method, which consists in defining a similar discrete problem, over a finite subspace V_h of the Sobolev space $H_0^2(\Omega)$. The associated discrete problem for (10) is: find $v_h \in V_h$ such that

$$a(v_h,u_h) = L(u_h) \quad \forall \ u_h \in V_h \tag{11}$$

which leads to solve a linear system over the space V_h. The finite element method is characterized by three aspects in the construction of the space V_h:

- A tessellation is established over the set $\Omega = [0,1] \times [0,1]$.

- The functions $v_h \in V_h$ are piecewise polynomials.

- There exists a basis in the space V_h whose functions have small support.

Details on the tessellation of the domain Ω and the construction of the subspace V_h with the Bogner-Fox-Schmit (BFS) elements are given in the appendix. Expressing $v_h \in V_h$ in the BFS basis leads to the identity:

$$v_h = \sum_{i,j=0}^{N_s-1,N_r-1} v_h(a_{ij})\varphi_{ij} + \frac{\partial v_h}{\partial s}(a_{ij})\psi_{ij} + \frac{\partial v_h}{\partial r}(a_{ij})\eta_{ij} + \frac{\partial^2 v_h}{\partial s \partial r}(a_{ij})\zeta_{ij} \tag{12}$$

where $a_{ij} = (ih_s, jh_r)$ are the nodal points. Equation (12) gives us a C^1 analytic solution over the set Ω. Finally the solution of the discrete problem associated to the equation (1) is equivalent to a solution of the linear system:

$$A \cdot V = L \tag{13}$$

where the matrix A is symmetric, definite positive and tridiagonal per bloc. The reader can find all details on the variational problem and linear system (13) in the appendix.

6 Discretization of the evolution problem

After we discretized the problem (2) in space, we discretize it in time with a finite difference method. This leads to:

$$\begin{cases} \frac{V^t - V^{t-1}}{\tau} + A \cdot V^t = L_{V^{t-1}} \\ V^0 = v_0 \text{ initial estimation.} \end{cases} \tag{14}$$

where τ is the time step. Equation (14) can be rewritten:

$$(Id + \tau A) \cdot V^t = V^{t-1} + \tau L_{V^{t-1}} \tag{15}$$

Finally to find a solution to the equation (9) we have to solve a linear system $M \cdot V = N$ at each time step, for which the matrix $M = (Id + \tau A)$ is banded, symmetric and positive definite. This

linear system is solved with a Conjugate Gradient method, in which the solution V_{t-1} is taken as an initial guess at time t. This approach appears to have a faster convergence than a Cholesky factorization.

7 Elasticity and rigidity coefficients

The elasticity and rigidity coefficients $w_{k,l}$ have a very important role in the convergence process of the surface toward the image edges.

These coefficients have to be chosen in a correct way such that the internal energy (the terms of the energy E including a coefficient $w_{k,l}$) and the external energy $\int\int F(v)dsdr$ have the same magnitude. In this case a minimum of the energy E will be a trade-off between the internal and external energy, and the obtained surface will perfectly fit the edge points while being smooth and regular. But if the internal energy is preponderant, the surface will tend to collapse on itself without detecting any image edge, whereas in the opposite case (small internal energy) the surface will converge toward the image edges while being very rough.

To insure that both internal and external energy have the same order of magnitude we found that it is sufficient to chose the coefficients $w_{k,l}$ in a way that the linear system of equations (9) be well conditioned. This leads to:

$$w_{10} = w_{01} = h_s^2 h_r^2 \quad \text{and} \quad w_{20} = w_{11} = w_{02} = h_s^3 h_r^3$$

where h_s and h_r are the discretization step of Ω.

We set $w_{10} = w_{01}$ and $w_{20} = w_{11} = w_{02}$ since the 3D image data were isotropic and consequently all directions have the same weight.

8 The computation of the vector L

The vector $L(e_{ij}) = -\int_\Omega \nabla P\,(v_{t-1}(s,r))\,e_{ij}(s,r)\;dsdr$ (where $e_{ij} = (\varphi_{ij},\ \psi_{ij},\ \eta_{ij},\ \zeta_{ij})$ is detailed in the appendix) represents the contribution of the external forces which attract the surface toward the edges in the linear system we solve at each iteration. Thus, the more we weight the potential $P = -|\nabla \mathcal{I}|^2$ the more accurate is the result and the faster is the convergence.

Since the potential P is known only at integer values (discrete image data) we have to compute the $L(e_{ij})$ with a numerical integration. Consequently we compute ∇P at any point $(x, y, z) \in R^3$ by a trilinear interpolation of its eight neighbors.

To take into account all the contributions of the external forces, we modified the numerical integration formula such that every image point in the set $v([(i-1)h_s,(i+1)h_s]\times[(j-1)h_r,(j+1)h_r])$ will be taken into account in the computation of each term $L(e_{ij})$. This method allows us to do an "adaptative subdivision" of the rectangle $K_{ij} = [ih_s,(i+1)h_s]\times[jh_r,(j+1)h_r]$ without adding nodal points and consequently without increasing the size of the linear system we solve. This method significantly reduces the algorithmic complexity while increasing the accuracy and the convergence speed.

9 Inferring the differential structure from 3D images

In the previous sections we showed how to use the deformable surface to segment and fit some 3-D image edge points. In the following we assume that the surface has localized accurately the 3-D image edges, which means that we have reached a minimum of E. We now use this surface to compute the differential characteristics of the 3-D image surface boundary. This computation can be done analytically at each point of the surface since the use of FEM gives us an analytic

representation of the surface $v(s,r)$:

$$v = \sum_{i,j=0}^{N_s-1,N_r-1} v_h(a_{ij})\varphi_{ij} + \frac{\partial v_h}{\partial s}(a_{ij})\psi_{ij} + \frac{\partial v_h}{\partial r}(a_{ij})\eta_{ij} + \frac{\partial^2 v_h}{\partial s \partial r}(a_{ij})\zeta_{ij} \tag{16}$$

where $\varphi_{ij}, \psi_{ij}, \eta_{ij}$ and ζ_{ij} are the basis functions and the coefficients $v_h(a_{ij})$, $\frac{\partial v_h}{\partial s}(a_{ij})$, $\frac{\partial v_h}{\partial r}(a_{ij})$ and $\frac{\partial^2 v_h}{\partial s \partial r}(a_{ij})$ are computed by solving the linear system (14). Another major contribution of the analytic representation is that at each point of the surface the tangent plane is given by the vectors $v_s = \frac{\partial v}{\partial s}$ and $v_r = \frac{\partial v}{\partial r}$ [3]. This allows us to compute all the differential characteristics in local coordinates, and consequently handle more general situations. Let us consider the basis $\{v_s, v_r, N\}$ where $N = \frac{v_s \wedge v_r}{|v_s \wedge v_r|}$, and let $T_p(\mathcal{S})$ denotes the tangent plane to $\mathcal{S}$ at the point $p \in R^3$. Since N_s and N_r belong to $T_p(\mathcal{S})$ we can write

$$\begin{aligned} N_s &= a_{11}v_s + a_{12}v_r \\ N_r &= a_{21}v_s + a_{22}v_r \end{aligned}$$

and therefore dN_p, which denotes the differential of N computed at point p, is given by the matrix $(a_{ij})_{i,j=1..2}$ in the basis $\{v_s, v_r, N\}$. This matrix can be expressed in terms of the first and second fundamental forms of $\mathcal{S}$ in the following way [10].

$$\begin{pmatrix} a_{11} & a_{12} \\ a_{21} & a_{22} \end{pmatrix} = \frac{-1}{EG - F^2} \begin{pmatrix} e & f \\ f & g \end{pmatrix} \begin{pmatrix} G & -F \\ -F & E \end{pmatrix}$$

where E, F, G, e, f and g are the coefficients of the first and second fundamental form in the basis $\{v_s, v_r, N\}$ defined by:

$$E = < v_s, v_s >, \quad F = < v_s, v_r >, \quad G = < v_r, v_r >$$

$$e = < N, v_{ss} >, \quad f = < N, v_{sr} >, \quad g = < N, v_{rr} >$$

[3] In the following the subscripts s,r,ss,rr and sr denote the first and second derivatives.

This gives us the relations:

$$\begin{aligned} a_{11} &= \frac{fF - eG}{EG - F^2} \quad a_{12} = \frac{gF - fG}{EG - F^2} \\ a_{21} &= \frac{eF - fE}{EG - F^2} \quad a_{22} = \frac{fF - gE}{EG - F^2} \end{aligned}$$

known as the *equations of Weingarten*. Thus the Gaussian curvature K and the mean curvature H of $\mathcal{S}$ at p are:

$$K = det(dN_p) = det(a_{ij}) = \frac{eg - f^2}{EG - F^2} \qquad H = -\frac{1}{2}(a_{11} + a_{22}) = \frac{1}{2}\frac{eG - 2fF + gE}{EG - F^2}$$

The principal curvatures are the negative eigenvalues of dN, they satisfy the equation:

$$det(dN_p + kI) = k^2 - 2Hk + K = 0 \quad \text{and therefore} \quad k = H \pm \sqrt{H^2 - K}$$

These equations give us a systematic method for classifying the points p of the surface in different classes:

- Elliptic if $det(dN_p) > 0$
- Hyperbolic if $det(dN_p) < 0$
- Parabolic if $det(dN_p) = 0$ with $dN_p \neq 0$
- Planar if $dN_p = 0$
- Umbilic if $k_1 = k_2$.

Thus for computing these characteristics we have to compute the first and the second fundamental forms of the surface. The surface $v(s, r)$ is C^∞ within each finite element patch but only C^1 along the isoparametric curves $s = ih_s$ or $r = jh_r$. Therefore, in the following experiments, the number of nodal points is about 600 ($N_s \simeq 30$ and $N_r \simeq 20$) for a surface which fits approximately 210×60 data points. This gives the ability to compute the coefficients of the second fundamental form over more than 6000 data points, whereas only the coefficients of the first fundamental form and

the coefficient f of the second fundamental form can be computed over the totality of the data points[4]. If absolutely necessary, we could convolve the second derivatives in the neighborhood of the isoparametric curves, with a gaussian filter to insure a $\mathcal{C}^2$ continuity everywhere.

10 Experimental results

Using a real 3-D deformable model to segment a 3-D image provides better results than the iterated application of a 2-D deformable model to successive 2-D cross-sections. In effect, the 3-D model easily brides edge gaps in 3-D, i.e. not only within a cross section, but also between cross-sections, insuring that the result is globally a smooth surface, and not only a collection of smooth planar curves. This significantly improves the robustness of the segmentation; for instance it is even possible to remove all the edges of a single cross section (assuming that the edges are correctly detected in the other ones) without degrading too much the final result.

We present in Figure 3 an example with artificial data. The 3D image here is a cylinder where we have removed some edges in 3 successives cross sections, to compare the results obtained by a 2-D model applied to successive cross sections with a full 3-D deformable model. With the deformable surface we can restore the lost edges and obtain a perfect reconstruction of the cylinder (Figure 3), whereas a 2-D model [8] cannot restore the lost edges even if we use the same attraction force as for the 3-D model.

We present now a typical example, with real data. Figure 4 shows a set of significant cross-sections of a vertebra (out of a total of 40 cross-sections), obtained with a X-ray scanner[5] and the initial segmentation provided by the user (the external curves show the intersection of the given

[4] the computation of f involves the cross derivative $v_{,rr}$ which is a component of the Bogner-Fox-Schmit basis, and hence is computed at the nodal points directly by solving the linear system (15).

[5] a courtesy of Pr. J.L. Coatrieux

surface with the corresponding cross-sections).

Figure 5 shows the resulting surface obtained after 40 iterations, in the same set of cross-sections. It is interesting to notice the remarkable accuracy of the segmentation, although the detected contours were often incomplete (due to noise effect). Figure 6 shows a wire-frame representation of the resulting surface[6].

We also present another typical example with real data. Figures 7 and 9 present some cross-sections of a human head (out of 70) obtained with Magnetic Resonance Imaging (MRI)[7]. Figures 8 and 9 show some cross sections of two different surfaces with the 2-D images. We remark the accurate localization by the surface of the 3-D edges. A wire-frame representation of these surfaces is given in figure 10.

Figure 11 represents some cross sections of the 3D edge image of a human heart (obtained with MRI) with the initial surface (in grey). Figure 12 shows some cross sections of the surface, once it has reached the minimum of E. We can notice the good localization of the surface on the 3D edge points. Figure 13 gives a 3D representation of the inside cavity of the left ventricle.

11 Conclusion and future research

We have shown how a deformable surface can be used to segment 3-D images by minimizing an appropriate energy. The minimization process is done by a variational method with finite elements. The use of finite elements method has some advantages compared to the finite difference method:

1. it requires less discretization points and consequently produces smaller linear system to solve, thus reducing significantly the algorithmic complexity.

[6] Obtained with the modeller of Chakib Bennis at INRIA.

[7] by courtesey of General-Electric CGR.

2. it produces more accurate results since the external forces can be computed more accurately,

3. it provides an analytical representation of the surface.

This last feature is the most important one for inferring differential structures of the surface, and we showed how to compute the first and second fundamental forms of the deformable model. These characteristics provide a helpful tool for recognizing 3D objects. They will be used soon to match the deformable surface to an anatomical atlas [2].

12 Appendices

A Surfaces and 3D edge points

In this first appendix we give a necessary and sufficient condition for a surface to produce a local extremum of the energy:

$$E_P(\mathcal{S}) = -\frac{1}{|\mathcal{S}|}\int\int |\nabla \mathcal{I}(\boldsymbol{x}(s,r))|\, ds dr$$

where $|\mathcal{S}| = \int\int ds dr$. A necessary and sufficient condition for the surface $\mathcal{S}$ to produce a local extremum of E_P with respect to infinitesimal deformations is:

$$\frac{d\,|\nabla \mathcal{I}(\boldsymbol{x}(s,r))|}{dN(\boldsymbol{x}(s,r))} = \frac{eG+gE}{EG}\left(|\nabla \mathcal{I}(\boldsymbol{x}(s,r))| - \frac{1}{|\mathcal{S}|}\int\int |\nabla \mathcal{I}(\boldsymbol{x}(s,r))|\, ds dr\right) = 0, \qquad (17)$$

and

$$P(\boldsymbol{x}(L,r)) = P(\boldsymbol{x}(0,r)) = \frac{1}{|\mathcal{S}|}\int\int P ds dr \quad \forall r \in [0,M] \qquad (18)$$

$$P(\boldsymbol{x}(s,M)) = P(\boldsymbol{x}(s,0)) = \frac{1}{|\mathcal{S}|}\int\int P ds dr \quad \forall s \in [0,L] \qquad (19)$$

where $E(s,r)$, $G(s,r)$, $e(s,r)$ and $g(s,r)$ are the coefficients of the first and second fundamental form in the basis $\{\boldsymbol{x}_s, \boldsymbol{x}_r\}$ (see [10] for details about the notations),$\Omega = [0,L]\times[0,M]$ and $P = |\nabla \mathcal{I}|$.

Let us consider $\mathcal{S}_\lambda$ a small deformation of the surface $\mathcal{S}$ such that the parametrization of $\mathcal{S}_\lambda$ is:

$$\boldsymbol{x}^\lambda = \boldsymbol{x} + \lambda(\alpha \boldsymbol{x}_s + \beta \boldsymbol{x}_r + \gamma N) \qquad (20)$$

where $\alpha(s,r)$, $\beta(s,r)$ and $\gamma(s,r)$ are arbitrary continuous and differentiable functions and $\{x_s, x_r, N\}$ are the derivatives of x and the normal to the surface.

$\mathcal{S}$ is a local extremum of E_P if and only if

$$\left.\frac{dE_P(\mathcal{S}_\lambda)}{d\lambda}\right|_{\lambda=0} = 0 \tag{21}$$

for all α, β and γ.

We are going to show that (21) holds if and only if (17, 18, 19) are satisfied.

By definition

$$E_P(\mathcal{S}_\lambda) = -\frac{\int\int_{\Omega_\lambda} P(x^\lambda(s_\lambda, r_\lambda))ds_\lambda dr_\lambda}{\int\int_{\Omega_\lambda} ds_\lambda dr_\lambda} \tag{22}$$

where $(s_\lambda, r_\lambda) \in \Omega_\lambda$ are the parametrization variables of $\mathcal{S}_\lambda$. Let $h : \Omega \to \Omega_\lambda$ such that $h(s,r) = (s_\lambda, r_\lambda)$. Since the variables s and r are independent the Jacobian $J_h = \left|x_s^\lambda\right| \left|x_r^\lambda\right|$. Hence

$$E_P(\mathcal{S}_\lambda) = -\frac{\int\int_{\Omega} P(x^\lambda \circ h(s,r))dsdr}{\int\int_{\Omega} J_h dsdr}. \tag{23}$$

To compute the derivative $\left.\frac{dE_P(\mathcal{S}_\lambda)}{d\lambda}\right|_{\lambda=0}$, we need to compute the derivatives of the vectors x_s, x_r and N. For this purpose we use the following equations (§ 4.3 p. 231 in [10]):

$$x_{ss} = \Gamma_{11}^1 x_s + \Gamma_{11}^2 x_r + eN$$

$$x_{sr} = x_{rs} = \Gamma_{12}^1 x_s + \Gamma_{12}^2 x_r + fN$$

$$x_{rr} = \Gamma_{22}^1 x_s + \Gamma_{22}^2 x_r + gN$$

where the coefficients Γ_{ij}^k are the Christoffel symbols of $\mathcal{S}$ in the parametrization x and where e, f, g are the coefficients of the second fundamental form of $\mathcal{S}$. In the following the Christoffel symbols Γ_{ij}^k have been replaced in terms of the coefficients of the first fundamental form E, F, G and their derivatives.

Thus computing $\frac{dE_P(\mathcal{S}_\lambda)}{d\lambda}$ and evaluating it at $\lambda = 0$ leads to:

$$
\begin{aligned}
|\mathcal{S}| \left.\frac{dE_P(\mathcal{S}_\lambda)}{d\lambda}\right|_{\lambda=0} = 0 \quad = \quad & \int\int \alpha \left[\frac{dP}{dx_s}\sqrt{EG} + \frac{1}{2}(P - P_m)\left(E_s\sqrt{\frac{G}{E}} + G_s\sqrt{\frac{E}{G}} \right) \right] dsdr \\
& + \int\int \alpha_s \sqrt{EG}(P - P_m)\, dsdr + \int\int \alpha_r F \sqrt{\frac{E}{G}}(P - P_m)\, dsdr \\
& + \int\int \beta \left[\frac{dP}{dx_r}\sqrt{EG} + \frac{1}{2}(P - P_m)\left(E_r\sqrt{\frac{G}{E}} + G_r\sqrt{\frac{E}{G}} \right) \right] dsdr \\
& + \int\int \beta_r \sqrt{EG}(P - P_m)\, dsdr + \int\int \beta_s F \sqrt{\frac{G}{E}}(P - P_m)\, dsdr \\
& + \int\int \gamma \left[\frac{dP}{dN}\sqrt{EG} - (P - P_m)\frac{eG + gE}{\sqrt{EG}} \right] dsdr
\end{aligned}
$$

where $P_m = \frac{1}{|\mathcal{S}|}\int\int P dsdr$.

Integrating by parts the integral (except the last one) yields (17) as a necessary and sufficient condition for (21) to be satisfied for all α, β and γ. And evaluating these integrals at the boundaries yields the two additional equations (18) and (19).

B Details on the numerical solution

B.1 Variational formulation

Let $\varphi \in H_0^2(\Omega)$ be a smooth function. If v is a solution of equation (9), we have:

$$
\begin{aligned}
\int_\Omega \frac{\partial v}{\partial t}\varphi dsdr - \int_\Omega \frac{\partial}{\partial s}\left(w_{1,0}\frac{\partial v}{\partial s} \right)\varphi dsdr - \int_\Omega \frac{\partial}{\partial r}\left(w_{0,1}\frac{\partial v}{\partial r} \right)\varphi dsdr + 2\int_\Omega \frac{\partial^2}{\partial s \partial r}\left(w_{1,1}\frac{\partial^2 v}{\partial s \partial r} \right)\varphi dsdr \\
+ \int_\Omega \frac{\partial^2}{\partial s^2}\left(w_{2,0}\frac{\partial^2 v}{\partial s^2} \right)\varphi dsdr + \int_\Omega \frac{\partial^2}{\partial r^2}\left(w_{0,2}\frac{\partial^2 v}{\partial r^2} \right)\varphi dsdr = -\int_\Omega \nabla P(v)\varphi dsdr
\end{aligned}
$$

where the function v depends on t, s and r. We remark that the variable t does not depend on s and r, thus we can separate them (for more details see [6]). The Green's formula yields:

$$
\begin{aligned}
\frac{d}{dt}\int_\Omega v\varphi dsdr + \int_\Omega w_{1,0}\frac{\partial v}{\partial s}\frac{\partial \varphi}{\partial s}dsdr + \int_\Omega w_{0,1}\frac{\partial v}{\partial r}\frac{\partial \varphi}{\partial r}dsdr + 2\int_\Omega w_{1,1}\frac{\partial^2 v}{\partial s \partial r}\frac{\partial^2 \varphi}{\partial s \partial r}dsdr \\
+ \int_\Omega w_{2,0}\frac{\partial^2 v}{\partial s^2}\frac{\partial^2 \varphi}{\partial s^2}dsdr + \int_\Omega w_{0,2}\frac{\partial^2 v}{\partial r^2}\frac{\partial^2 \varphi}{\partial r^2}dsdr = -\int_\Omega \nabla P(v)\varphi dsdr
\end{aligned}
$$

Let us set:

$$a(u,v) = \int_\Omega w_{10}\frac{\partial u}{\partial s}\frac{\partial v}{\partial s} + w_{01}\frac{\partial u}{\partial r}\frac{\partial v}{\partial r} + w_{20}\frac{\partial^2 u}{\partial s^2}\frac{\partial^2 v}{\partial s^2} + 2w_{11}\frac{\partial^2 u}{\partial s \partial r}\frac{\partial^2 v}{\partial s \partial r} + w_{02}\frac{\partial^2 u}{\partial r^2}\frac{\partial^2 v}{\partial r^2}\, dsdr$$

and

$$L(u) = -\int_\Omega \nabla P\, u\, dsdr$$

This leads to a new formulation of the problem: given $v_0 \in L^2(\Omega)$ and $\nabla P \in L^2(0,T,L^2(\Omega))$, find a function $v \in L^2(0,T,H_0^2(\Omega)) \cap C^1(0,T,L^2(\Omega))$ satisfying:

$$\begin{cases} \frac{d}{dt}(v(t),\psi) + a(v(t),\psi) = L(\psi)\ \forall \psi \in H_0^2(\Omega) \\ v(0) = v_0(s,r) \\ w_{i,j} \in L^\infty(\Omega) \ \text{ and } w_{i,j}(s) \geq \alpha > 0 \end{cases} \tag{24}$$

Since the variables s, r and t are independent, we can solve equation (24) in two steps: first solve the static equation: find $v \in H_0^2(\Omega)$ such that

$$a(v,\varphi) = L(\varphi) \quad \forall \varphi \in H_0^2(\Omega) \tag{25}$$

where L is not supposed to depend on v (we remind the reader that there exists a unique solution to this equation, since the bilinear form $a(\varphi,\psi)$ is symmetric and positive definite as long as $w_{i,j} > 0$), and then solve the evolution equation (24). This yields the equation (15).

B.2 Tessellation of Ω and the basis functions

Given the numbers of discretization points in the two axes of parametrization N_s, $N_r > 1$, we set $h_s = \frac{1}{N_s - 1}$, $h_r = \frac{1}{N_r - 1}$ and consider a uniform subdivision of Ω of step size h_s and h_r, composed of the nodes $a_{i,j} = (x_i, y_j) = (ih_s, jh_r)$ $0 \leq i \leq N_s - 1$, $0 \leq j \leq N_r - 1$. Thus

$$\Omega = [0,1] \times [0,1] = \bigcup_{i,j=0}^{N_s-1,N_r-1} K_{i,j} = \bigcup_{i,j=0}^{N_s-1,N_r-1} [ih_s,(i+1)h_s] \times [jh_r,(j+1)h_r]$$

Since the higher derivatives order appearing in the equation (1) are of the fourth order, the finite element space V_h must satisfy $V_h \subset \mathcal{C}^1 \cap H_0^2(\Omega)$ (see for details [6]). For this purpose the space $H_0^2(\Omega)$ is approximated with the Bogner - Fox - Schmit elements [6] defined by:

- The rectangles K_{ij}, defined by the vertices $c_k \;\; 1 \leq k \leq 4$.
- The set $P_{K_{ij}}$ of polynomials containing the basis functions:

$$P_{K_{ij}} = Q_3(R^2) = \left\{ p, \;\; p(s,r) = \sum_{\alpha_i \leq 3, \;\; 1 \leq i \leq 2} \gamma_{\alpha_1 \alpha_2} s^{\alpha_1} r^{\alpha_2} \right\}$$

- The set $\Sigma_{K_{ij}} = \left\{ p(c_k), \; \frac{\partial p(c_k)}{\partial s}, \; \frac{\partial p(c_k)}{\partial r}, \; \frac{\partial^2 p(c_k)}{\partial s \partial r} \quad 1 \leq k \leq 4 \right\}$ which allows to define in a unique way the basis functions over each rectangles K_{ij}

The subspace V_h is then defined by:

$$V_h = \left\{ v \in \mathcal{C}^1(\Omega), \;\; v_{|K_{ij}} \in Q_3(K_{ij}) \right\}$$

where $Q_k(I)$ is the vector space of the restrictions to an interval $I \subset R^2$ of the polynomials whose degree is less than k for each variable, and $v_{|I}$ is the restriction of the function v to the subset I. The basis functions of the finite element subspace V_h are φ_{ij}, ψ_{ij}, η_{ij} and ζ_{ij} defined in a unique way over each rectangle K_{ij} by:

$$\left\{ \begin{array}{lllllllll}
\varphi_{ij}(a_{kl}) & = & \delta_{ij,kl}; & \frac{\partial \varphi_{ij}}{\partial s}(a_{kl}) & = & \frac{\partial \varphi_{ij}}{\partial r}(a_{kl}) & = & \frac{\partial^2 \varphi_{ij}}{\partial s \partial r}(a_{kl}) & = 0 \\
\frac{\partial \psi_{ij}}{\partial s}(a_{kl}) & = & \delta_{ij,kl}; & \psi_{ij}(a_{kl}) & = & \frac{\partial \psi_{ij}}{\partial r}(a_{kl}) & = & \frac{\partial^2 \psi_{ij}}{\partial s \partial r}(a_{kl}) & = 0 \\
\frac{\partial \eta_{ij}}{\partial r}(a_{kl}) & = & \delta_{ij,kl}; & \eta_{ij}(a_{kl}) & = & \frac{\partial \eta_{ij}}{\partial s}(a_{kl}) & = & \frac{\partial^2 \eta_{ij}}{\partial s \partial r}(a_{kl}) & = 0 \\
\frac{\partial^2 \zeta_{ij}}{\partial s \partial r}(a_{kl}) & = & \delta_{ij,kl}; & \zeta_{ij}(a_{kl}) & = & \frac{\partial \zeta_{ij}}{\partial s}(a_{kl}) & = & \frac{\partial \zeta_{ij}}{\partial r}(a_{kl}) & = 0
\end{array} \right. \tag{26}$$

where:

$$\delta_{ij,kl} = \left\{ \begin{array}{ll} 1 & \text{if } i = k \text{ and } j = l \\ 0 & \text{otherwise} \end{array} \right.$$

Thus $\forall v_h \in V_h$ we have the identity:

$$v_h = \sum_{i,j=0}^{N_s-1,N_r-1} v_h(a_{ij})\varphi_{ij} + \frac{\partial v_h}{\partial s}(a_{ij})\psi_{ij} + \frac{\partial v_h}{\partial r}(a_{ij})\eta_{ij} + \frac{\partial^2 v_h}{\partial s \partial r}(a_{ij})\zeta_{ij}$$

providing a continuous representation of the solution over the space Ω.

Equations (26) gives the expressions of the basis functions φ_{ij}, ψ_{ij}, η_{ij} and ζ_{ij}. This leads to analytical expressions which are too long to be reported here. Instead, we give a graphical representation of them (Figure 1).

B.3 Discrete problem and linear system

Rewriting the discrete problem associated to equation (25) with the basis functions, gives us the four equations: $\forall i, j = 0, \ldots, N_s - 1, N_r - 1$

$$\begin{cases} a(v_h, \varphi_{ij}) = L(\varphi_{ij}) \\ a(v_h, \psi_{ij}) = L(\psi_{ij}) \\ a(v_h, \eta_{ij}) = L(\eta_{ij}) \\ a(v_h, \zeta_{ij}) = L(\zeta_{ij}) \end{cases} \tag{27}$$

and, using the identity (12): $\forall i, j = 0, \ldots, N_s - 1, N_r - 1$

$$\begin{cases} \sum_{k,l=0}^{N_s-1,N_r-1} v_h(a_{kl})a(\varphi_{kl}, \varphi_{ij}) + \frac{\partial v_h}{\partial s}(a_{kl})a(\varphi_{kl}, \psi_{ij}) + \frac{\partial v_h}{\partial r}(a_{kl})a(\varphi_{kl}, \eta_{ij}) + \frac{\partial^2 v_h}{\partial s \partial r}(a_{kl})a(\varphi_{kl}, \zeta_{ij}) = L(\varphi_{ij}) \\ \sum_{k,l=0}^{N_s-1,N_r-1} v_h(a_{kl})a(\psi_{kl}, \varphi_{ij}) + \frac{\partial v_h}{\partial s}(a_{kl})a(\psi_{kl}, \psi_{ij}) + \frac{\partial v_h}{\partial r}(a_{kl})a(\psi_{kl}, \eta_{ij}) + \frac{\partial^2 v_h}{\partial s \partial r}(a_{kl})a(\psi_{kl}, \zeta_{ij}) = L(\psi_{ij}) \\ \sum_{k,l=0}^{N_s-1,N_r-1} v_h(a_{kl})a(\eta_{kl}, \varphi_{ij}) + \frac{\partial v_h}{\partial s}(a_{kl})a(\eta_{kl}, \psi_{ij}) + \frac{\partial v_h}{\partial r}(a_{kl})a(\eta_{kl}, \eta_{ij}) + \frac{\partial^2 v_h}{\partial s \partial r}(a_{kl})a(\eta_{kl}, \zeta_{ij}) = L(\eta_{ij}) \\ \sum_{k,l=0}^{N_s-1,N_r-1} v_h(a_{kl})a(\zeta_{kl}, \varphi_{ij}) + \frac{\partial v_h}{\partial s}(a_{kl})a(\zeta_{kl}, \psi_{ij}) + \frac{\partial v_h}{\partial r}(a_{kl})a(\zeta_{kl}, \eta_{ij}) + \frac{\partial^2 v_h}{\partial s \partial r}(a_{kl})a(\zeta_{kl}, \zeta_{ij}) = L(\zeta_{ij}) \end{cases} \tag{28}$$

Equation (28) is a linear system where the unknowns are $v_h(a_{kl})$, $\frac{\partial v_h}{\partial r}(a_{kl})$, $\frac{\partial v_h}{\partial s}(a_{kl})$ and $\frac{\partial^2 v_h}{\partial s \partial r}(a_{kl})$.

Finally the solution of the discrete problem associated to (25) leads to a solution of a linear

system: $A \cdot V = L$, where: $A = (\tilde{A}_{ij})_{ij=0,\ldots,Ns-1,Nr-1}$ is a tridiagonal blocs array:

$$\tilde{A}_{ij} = \begin{pmatrix} a(\varphi_{ij},\varphi_{kl}) & a(\varphi_{ij},\psi_{kl}) & a(\varphi_{ij},\eta_{kl}) & a(\varphi_{ij},\zeta_{kl}) \\ a(\psi_{ij},\varphi_{kl}) & a(\psi_{ij},\psi_{kl}) & a(\psi_{ij},\eta_{kl}) & a(\psi_{ij},\zeta_{kl}) \\ a(\eta_{ij},\varphi_{kl}) & a(\eta_{ij},\psi_{kl}) & a(\eta_{ij},\eta_{kl}) & a(\eta_{ij},\zeta_{kl}) \\ a(\zeta_{ij},\varphi_{kl}) & a(\zeta_{ij},\psi_{kl}) & a(\zeta_{ij},\eta_{kl}) & a(\zeta_{ij},\zeta_{kl}) \end{pmatrix}$$

the $\tilde{A}_{ij}$ array elements depend on the elasticity and rigidity coefficients.

Acknowledgements

We thank Chakib Bennis who provide the modeller for the wire-frame representations of the surfaces.

References

[1] N. Ayache, J.D. Boissonnat, E. Brunet, L. Cohen, J.P. Chièze, B. Geiger, O. Monga, J.M. Rocchisani, and P. Sander. Building highly structured volume representations in 3d medical images. In *Computer Aided Radiology*, 1989. Berlin, West-Germany.

[2] N. Ayache, J.D. Boissonnat, L. Cohen, B. Geiger, J. Levy-Vehel, O. Monga, and P. Sander. Steps toward the automatic interpretation of 3-d images. In H. Fuchs K. Hohne and S. Pizer, editors, *3D Imaging in Medicine*, pages 107–120. NATO ASI Series, Springer-Verlag, 1990.

[3] Gunilla Borgefors. Distance transformations in arbitrary dimensions. *Computer Vision, Graphics, and Image Processing*, 27:321–345, 1984.

[4] Michael Brady, Jean Ponce, Alan Yuille, and Haruo Asada. Describing surfaces. In Hideo Hanafusa and Hirochika Inoue, editors, *Proceedings of the Second International Symposium on Robotics Research*, pages 5–16, Cambridge, Mass., 1985. MIT Press.

[5] John Canny. A computational approach to edge detection. *IEEE Transactions on Pattern Analysis and Machine Intelligence*, PAMI-8(6):679–698, November 1986.

[6] P. G. Ciarlet. *The finite element methods for elliptic problems.* NORTH-HOLLAND, 1987.

[7] L. Cohen. On active contour models and balloons. *CVGIP: Image understanding.* to appear, available as INRIA report 1075.

[8] Laurent D. Cohen and Isaac Cohen. A finite element method applied to new active contour models and 3d reconstruction from cross sections. In *Proceedings of the third International Conference on Computer Vision*, December 1990.

[9] P. E. Danielsson. Euclidean distance mapping. *Computer Vision, Graphics, and Image Processing*, 14:227–248, 1980.

[10] Manfredo P. do Carmo. *Differential Geometry of Curves and Surfaces.* Prentice-Hall, Englewood Cliffs, 1976.

[11] Pascal Fua and Yvan G. Leclerc. Model driven edge detection. In *DARPA Image Understanding Workshop*, 1988.

[12] Michael Kass, Andrew Witkin, and Demetri Terzopoulos. Snakes: Active contour models. In *Proceedings of the First International Conference on Computer Vision*, pages 259–268, London, June 1987.

[13] Olivier Monga and Rachid Deriche. 3d edge detection using recursive filtering. In *Conference on Vision and Patern Recognition*, San Diego, June 1989. IEEE.

[14] J. Alison Noble. Finding corners. In *Proceedings of Alvey Vision Conference*, pages 267–274, June 1987.

[15] Jean Ponce and Michael Brady. Toward a surface primal sketch. In *Proceedings, IJCAI*, 1985.

[16] Peter T. Sander and Steven W. Zucker. Inferring surface trace and differential structure from 3-D images. *IEEE Transactions on Pattern Analysis and Machine Intelligence*, 1990. In the press. A shortened version is available as "Charting Surface Structure", in *Proceedings of the First European Conference on Computer Vision*, Antibes, April 23–27.

[17] Demetri Terzopoulos, Andrew Witkin, and Michael Kass. Constraints on deformable models: recovering 3d shape and nonrigid motion. *AI Journal*, 36:91–123, 1988.

[18] Demitri Terzopoulos Andrew Witkin and Michael Kass. Symmetry-seeking models for 3d object reconstruction. In *Proceedings of the first International Conference on Computer Vision*, pages 269–276, June 1987.

[19] S.W. Zucker and R.M. Hummel. A three-dimensional edge operator. *IEEE Transactions on Pattern Analysis and Machine Intelligence*, PAMI-3(3):324–331, May 1981.

C Figures

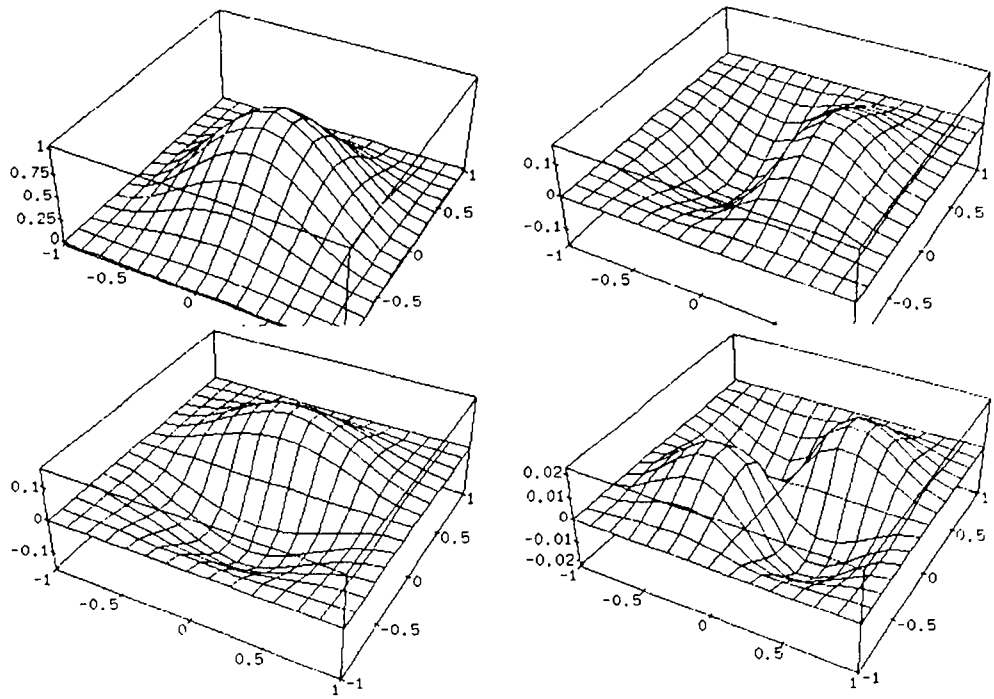

Figure 1: Representation of the four basis functions φ, ψ, η and ζ.

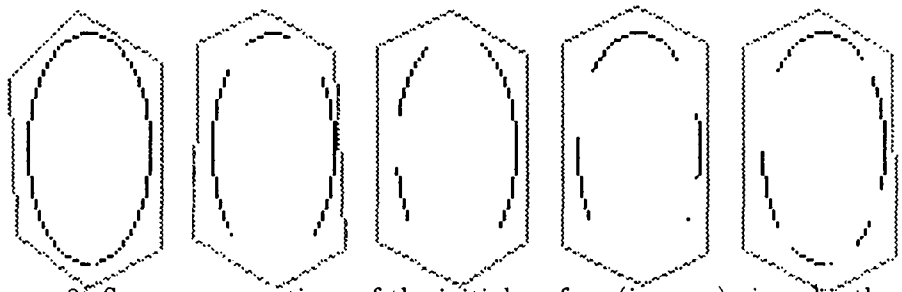

Figure 2: Some cross sections of the initial surface (in grey) given by the user

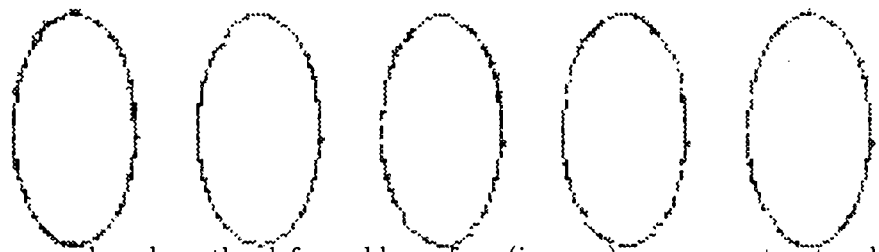

Figure 3: Here we show how the deformable surface (in grey) can reconstruct a deteriored edges while having a 3D homogeneity. In this example a 2D model cannot reconstruct the lost edges even if we use a 3D potential

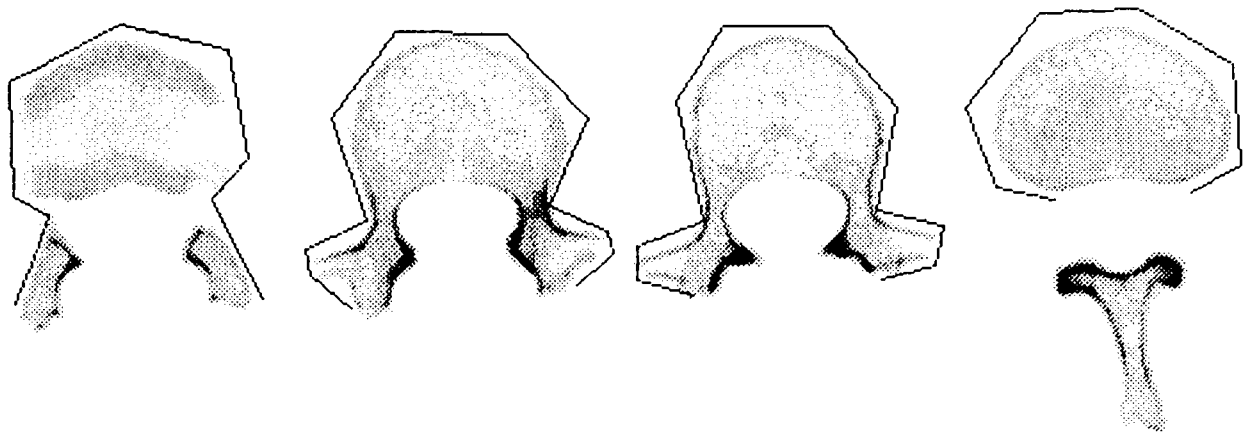

Figure 4: Some cross sections of the initial surface given by the user

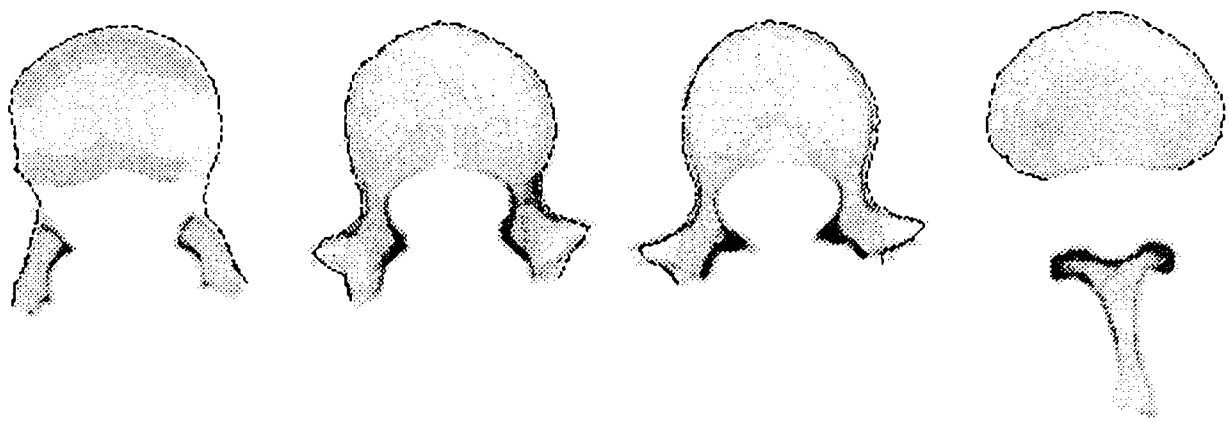

Figure 5: The corresponding cross sections of the solution

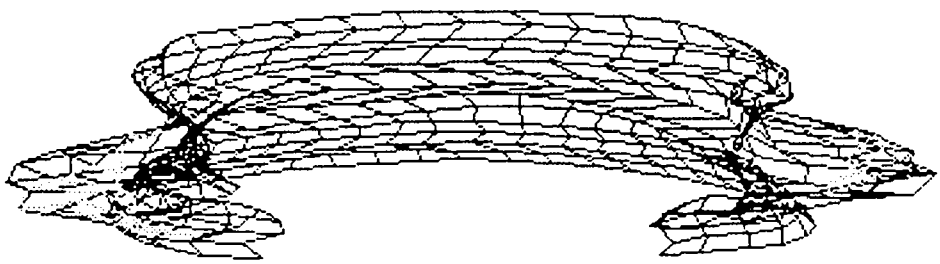

Figure 6: A wire-frame representation of the vertebra

Figure 7: Representation of some cross sections of the initial surface given by the user

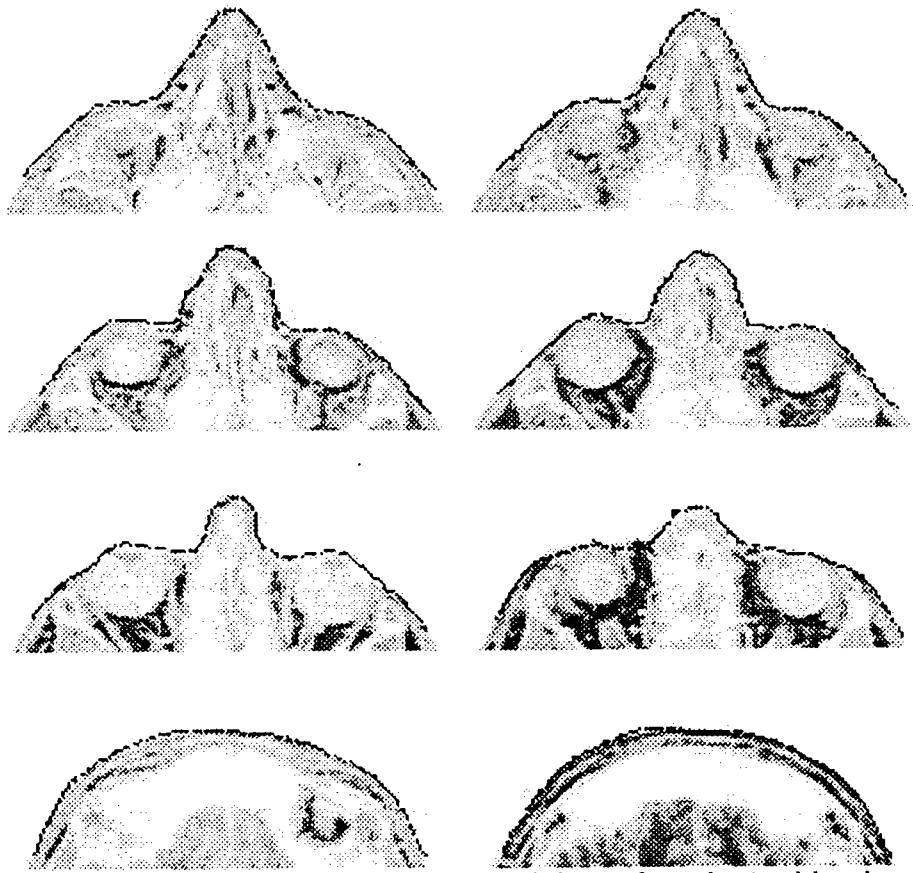

Figure 8: Representation of some cross sections of the surface obtained by the algorithm

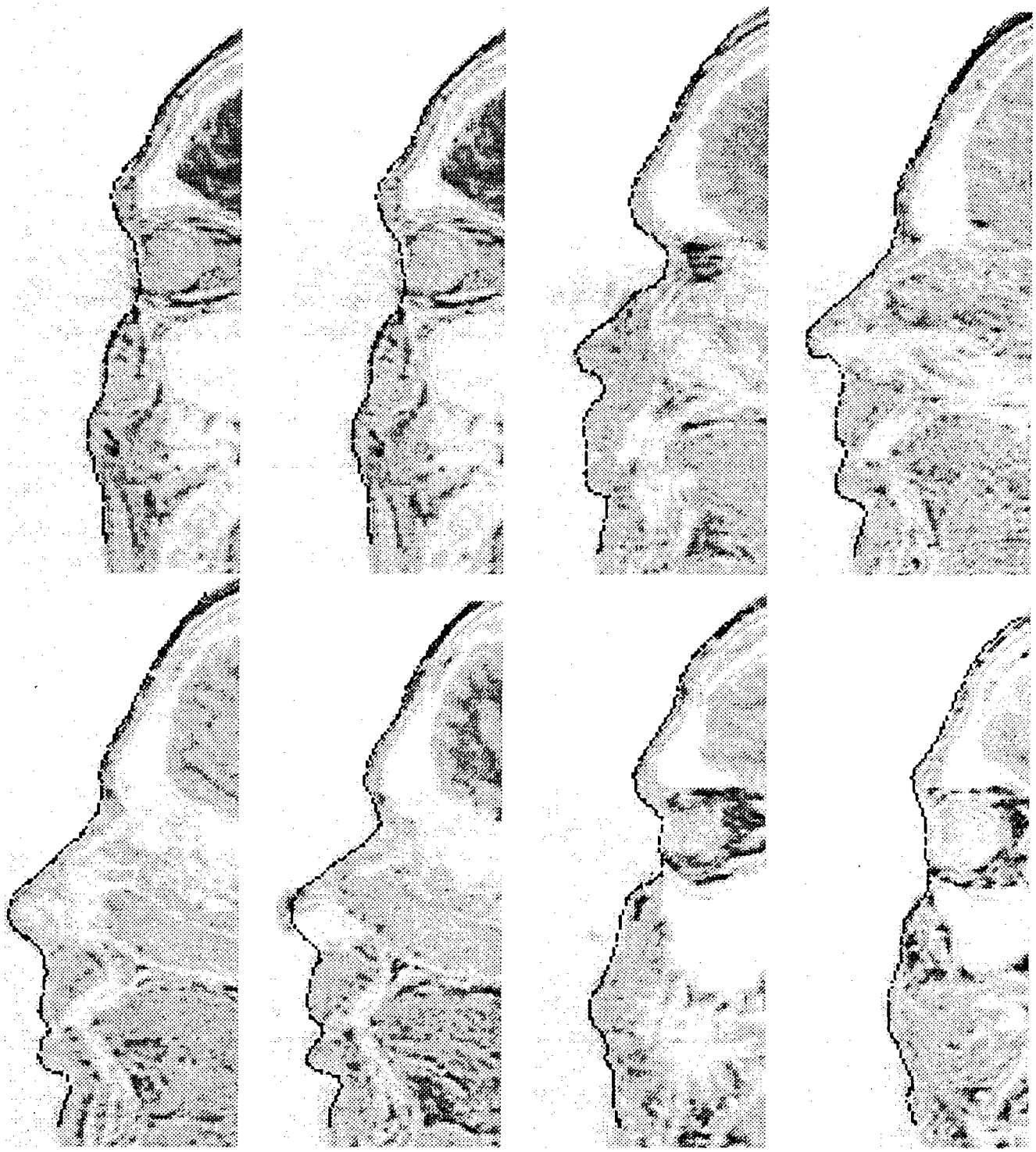

Figure 9: Another example, where the initial condition was similar to the one in the previous example

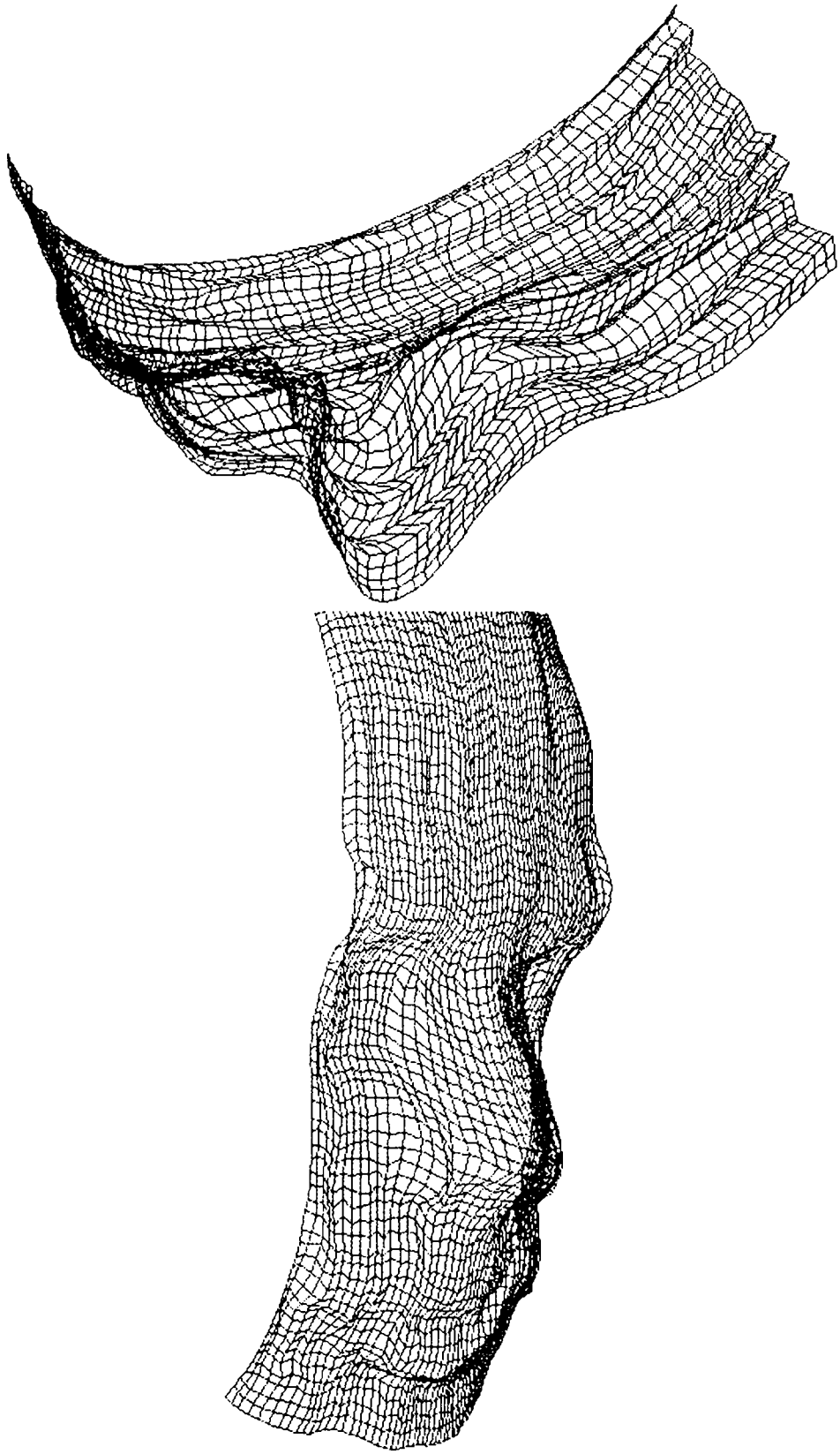

Figure 10: Two wire-frame representations of the surfaces corresponding to the previous examples

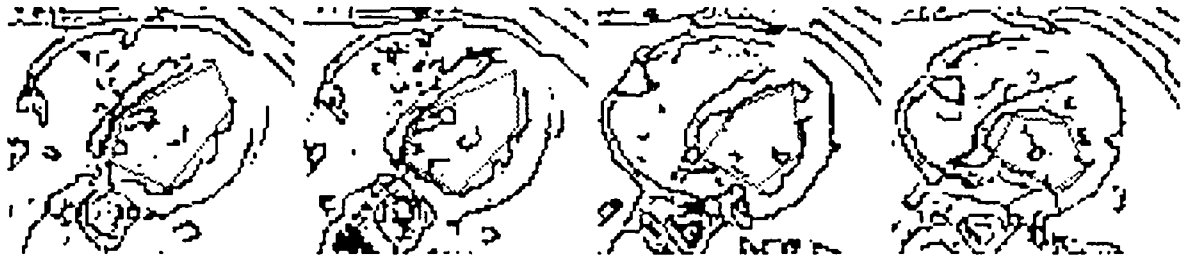

Figure 11: Some cross sections of the initial surface (in grey)

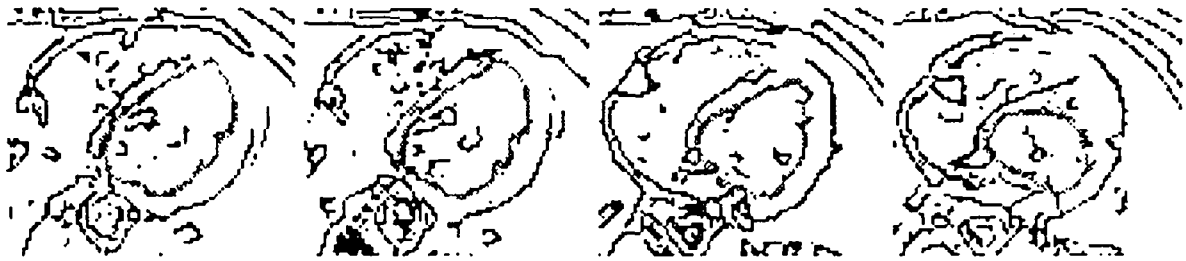

Figure 12: Here we give a further exemple where we use a deformable surface constrained by boundaries conditions (cylinder type) to segment the inside cavity of the left ventricle. The cross sections of the surface (in grey) are given here with the contour image to show the accurate localization of the surface.

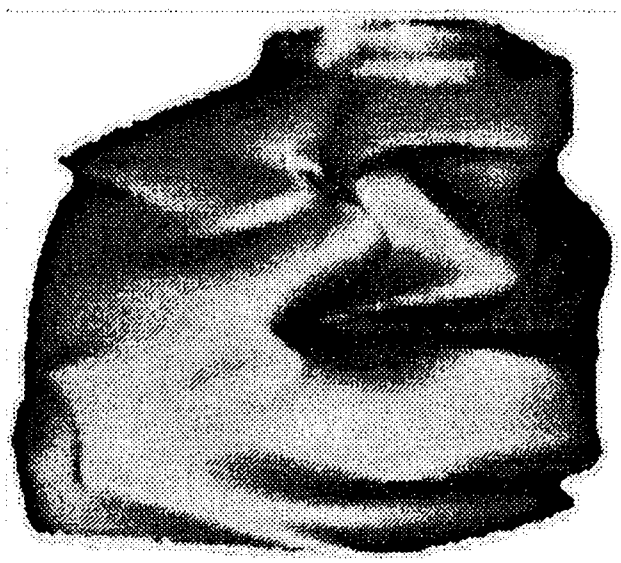

Figure 13: A representation of the inside surface of the left ventricle

Imprimé en France
par
. l'Institut National de Recherche en Informatique et en Automatique

ISSN 0249-6399